Pergamon

Acta mater. 49 (2001) 3269–3276

Acta MATERIALIA

www.elsevier.com/locate/actamat

ON THE ORIGIN OF DEFORMATION MICROSTRUCTURES IN AUSTENITIC STAINLESS STEEL: PART I—MICROSTRUCTURES

E. H. LEE†, T. S. BYUN, J. D. HUNN, M. H. YOO, K. FARRELL‡ and L. K. MANSUR

Metals and Ceramics Division, Oak Ridge National Laboratory, P.O. Box 2008, Oak Ridge, TN 37831-6376, USA

(Received 23 January 2001; accepted 11 May 2001)

Abstract—A comprehensive characterization of room temperature deformation microstructures was carried out by transmission electron microscopy for ion irradiated and deformed AISI 316LN austenitic stainless steel. Deformation microstructures were produced by a recently developed disk-bend test method and also by a uniaxial tensile test. Cross-slip was dramatically suppressed by the radiation-induced defects and slip occurred predominantly by planar glide of Shockley partial dislocations. Deformed microstructures consisted of piled-up dislocations, nanotwin layers, stacking faults, and defect-reduced dislocation channel bands. Analyses revealed that all these features were different manifestations of the same type of deformation band, namely a composite of overlapping faulted layers produced by Shockley partial dislocations. *© 2001 Acta Materialia Inc. Published by Elsevier Science Ltd. All rights reserved.*

Keywords: Steels (austenite); Deformation; Microstructure

1. INTRODUCTION

Plastic instability by strain localization has been identified as one of the potential causes of failure for AISI 316 type austenitic stainless steel under high stress, particularly for the components subjected to high doses of neutrons in fission and fusion reactors [1, 2], or protons and neutrons in spallation neutron sources [3]. In the past, for reasons of simplicity, deformation mechanisms for irradiated materials have been studied mostly for elemental metals, e.g. Al, Cu, Mo, Nb, Re, or simple alloys [4–9]. Only limited studies have been performed for irradiated austenitic stainless steels following deformation [1, 10–14]. In general, deformed microstructures of irradiated materials were characterized by localized pileup of dislocations and defect-reduced channels for f.c.c. metals with relatively high stacking fault energy such as Al (200–250 mJ/m^2) and Cu (40–90 mJ/m^2), and for b.c.c. metals such as Nb and Mo. For metals with low stacking fault energy such as austenitic stainless steels (<10 mJ/m^2), twin bands, associated stacking fault fringes and martensite lamellae are observed for the materials tested from room temperature to 450°C [1, 10–14].

In Ni-ion irradiated and deformed 304L austenitic stainless steel, it was reported that twinning was the dominant deformation mode at low temperature (25°C) or high strain rate test conditions, while dislocation channeling was favored at higher temperature (288°C) or slower strain rate test conditions [1, 11]. Twin bands were observed for 304 stainless steel neutron irradiated and tested at 450°C [10] and for neutron irradiated J316 austenitic stainless steel tested at 330°C [14]. In the latter work, defect-free channels and martensitic laths also were observed. No significant defect-reduced dislocation channels were developed during in situ deformation of proton-irradiated 304 austenitic stainless steel at room temperature, although some dislocation loops were sheared or eliminated by glide dislocations [12]. In the latter work, twin formation was not reported. Some of the above works suggest that twinning and channeling are temperature- or strain-rate dependent, or that deformation is dictated by different mechanisms at different temperature regimes or strain-rate conditions. However, a careful review of the previous data and the data obtained from this work indicates that twinning or channeling does not depend upon test temperature at least in the temperature range tested thus far, since both twin and channel are observed equally from room temperature to 450°C.

The purpose of the present work is to clarify the deformation mechanisms of austenitic stainless steel through a thorough characterization of deformation

† Now with Honeywell Electronic Materials, 1349 Moffett Park Drive, Sunnyvale, CA 94089, USA.

‡ To whom all correspondence should be addressed. Tel.: +1 (865) 574-5059; fax: +1 (865) 574-0641.

E-mail address: farrellk@ornl.gov (K. Farrell)

1359-6454/01/$20.00 © 2001 Acta Materialia Inc. Published by Elsevier Science Ltd. All rights reserved.
PII: S1359-6454(01)00193-8

microstructures by transmission electron microscopy (TEM) for AISI 316LN austenitic stainless steel irradiated with 360 keV He and/or 3.5 MeV Fe ions and deformed by a recently developed disk-bend test method [15, 16]. Uniaxial tensile tests were also conducted in parallel for comparison. In this work, examples are given to demonstrate that the various deformation microstructures described in the previous literature cited above can originate from one type of deformation band. Detailed evolution mechanisms of deformation microstructures are discussed in Part II of this paper (this issue).

2. EXPERIMENTAL

The material used in this experiment was AISI 316LN austenitic stainless steel (Jessop Steel Company Heat # 18474), 1050°C solution annealed for 30 min. The nominal composition of the alloy was, in wt%, 16.3 Cr, 10.2 Ni, 2.01 Mo, 1.75 Mn, 0.39 Si, 0.009 C, 0.11 N, 0.029 P with the balance Fe. Mechanically and electrochemically polished disks (3 mm diameter and 0.25 mm thickness) were irradiated at 200°C with beams of 180 keV H, 360 keV He and/or 3.5 MeV Fe ions using 0.4, 2.5 and 5 MV Van de Graaff accelerators, respectively. The ion energies were chosen to produce maximum damage and gas atom deposition near a depth of 700–800 nm, according to a depth calculation by the computer code, Stopping and Range of Ions in Matter (SRIM, 1998 version) [17]. The 3.5 MeV Fe ions caused displacement damage only, whereas the 360 keV He ions produced gas atom deposition as well as atomic displacements at a rate of $\simeq 7.5\times10^{-5}$ dpa/appm. A procedure to calculate dpa (displacements per atom) is described in Refs. [18, 19].

The irradiated disks were deformed by the disk bend method described in previous papers [15, 16]. In this procedure, the irradiated side of the 3 mm diameter disk is placed face-down onto the recessed shoulder of 1.6 mm diameter hole in an anvil, and is clamped with a screw with 1.1 mm diameter opening at the center. Through the opening, a tungsten carbide (WC) ball of 1 mm diameter was placed on the unirradiated side of the TEM disk. A load up to $\approx$30 N was applied on the disk through the WC ball at a strain rate of $\approx 10^{-2}$/s at room temperature until the plastic strain of the center region of the irradiated surface attained about 10%. A Tinius Olsen tensile machine operated in compression mode was used as the loading device.

For calculation of the strain at the irradiated surface, first the plastic strain in the ball contact area (unirradiated top surface) was determined by the empirical formula, $\varepsilon_{\mathrm{I}}^{\mathrm{P}} = 0.2(d_{\mathrm{p}}/D)$, derived by Tabor [20], where d_{p} is the optically determined indentation (plastic) diameter and D is the ball diameter. Next, the average (middle of the disk) plastic strain ($\varepsilon_z^{\mathrm{P}}$) was derived by the relation, $\varepsilon_z^{\mathrm{P}} = \ln(t_{\mathrm{o}}/t)$, where t_{o} and t are the thicknesses of the center region of the disk before and after deformation, respectively. The plastic thickness change was determined, after zeroing the load to eliminate the elastic component, from the readings of the displacement of the tensile machine cross-head bar in contact with the top of the WC ball and the displacement of a linear variable differential transducer (LVDT) placed underneath the TEM disk. Finally, the plastic strain of the irradiated surface ($\varepsilon_{\mathrm{s}}^{\mathrm{P}}$) was determined from the relation of $\varepsilon_{\mathrm{s}}^{\mathrm{P}} = 2\varepsilon_z^{\mathrm{P}} - \varepsilon_{\mathrm{I}}^{\mathrm{P}}$. A detailed theoretical model analyzing the stress–strain for this disk bend technique is described in a separate paper [16].

Here, it should be pointed out that, despite the effort to determine the strain level as precisely as possible, the strains applied at the microstructural level varied considerably not only from grain to grain but also from area to area in the same grain. This was mainly due to the differences in grain orientations relative to the stress direction, non-uniform distribution of preexisting dislocations and Frank–Read sources in the grains, and differences in dislocation generating capacity of grain boundaries (e.g., low- vs high-angle grain boundaries and their relative orientation to the stress direction).

The irradiated and deformed specimens were thinned for TEM examination, first by electrochemically removing a $\simeq$700 nm thick surface layer from the irradiated side of the disk and then thinning from the unirradiated side until a perforation occurred. In this way, TEM foils with thicknesses of $\simeq$100 nm on average were prepared and the deformed microstructures were examined at the peak damage region between 700 and 800 nm from the original surface. This procedure allowed us to avoid any leakage of point defects to the specimen surface due to the diffusion during irradiation. A calculation based on a rate theory model showed that point defects at this depth would not be affected by the free surface, particularly at low temperature and high sink density conditions, since most point defects were recombined or captured by sinks within a much shorter diffusion mean free path than the distance between the peak damage region and the surface [21]. Therefore, the microstructures observed in this report are considered to represent bulk phenomena. In fact, in a previous experiment, no apparent surface effects were observed in the peak damage region during a cross-sectional examination of an irradiated and deformed 316LN steel [15].

Finally, a tensile specimen was irradiated to 10 dpa at 200°C with 3.5 MeV Fe ions and simultaneously with 360 keV He (200 appm/dpa) and 180 keV H (1000 appm/dpa) and then strained 20% at room temperature. TEM specimens were prepared from both unirradiated and irradiated sides of the tensile bar, following the same thinning procedure described above. Microstructures of both disk bend tested and tensile tested specimens were examined with a Philips CM12 electron microscope operated at 120 keV.

3. RESULTS AND ANALYSES

Before examining the deformed microstructures, the radiation-induced defects in as-irradiated specimens were characterized to identify the sources affecting subsequent deformation. Small black dots (vacancy and interstitial clusters <5 nm in diameter), larger interstitial type faulted Frank loops (Burgers vector $\mathbf{b} = \langle 111 \rangle/3$ type) and some unfaulted prismatic loops ($\mathbf{b} = \langle 110 \rangle/2$ type) were present in the specimen irradiated to 10 dpa at 200°C with 3.5 MeV Fe ions, as shown in Fig. 1. For simplicity, the unit lattice parameter '**a**' is omitted in all Burgers vector notations in this paper. In 360 keV He irradiated specimens, helium bubbles were observed in addition to loops (mostly faulted). However, the defect clusters and loops were noticeably smaller in size but more numerous compared to those in the Fe irradiated specimen. Figure 2 shows the loop and bubble microstructures for the specimens irradiated to 5 at.% He (3.75 dpa) and 10 at.% He (7.5 dpa) at 200°C with 360 keV He. In the 3.5 MeV Fe irradiated specimen, the number densities for black dots and Frank loops were of order $1\text{–}2\times10^{23}\ \mathrm{m}^{-3}$ and $2\text{–}3\times10^{22}\ \mathrm{m}^{-3}$, respectively. Bubbles were not visible below 1 at.% helium level, but the high helium microstructures indicated that the bubble and loop (including black dots) number densities tended to saturate at $2\text{–}6\times10^{26}\ \mathrm{m}^{-3}$ and $2\text{–}4\times10^{23}\ \mathrm{m}^{-3}$, respectively. Detailed descriptions of as-irradiated microstructures can be found elsewhere [22, 23].

During deformation of unirradiated austenitic stainless steel, cross-slip occurred readily resulting in fairly homogeneous distribution of dislocations in the grains, although there was a tendency to develop an equiaxed dislocation cell structure at low strain level due to the active polyslip system in f.c.c. crystals. In contrast, cross-slip was dramatically suppressed in the presence of radiation-induced defects such as loops and bubbles, and dislocation motion was restricted largely to widely spaced {111} slip planes. Figure 3 shows the 10% disk-bend strained microstructures for the 316LN irradiated at 200°C to 10 dpa with (a) 3.5 MeV Fe and (b) 7.5 dpa (10 at.% He) with 360 keV He. The satellite spots in the diffraction pattern indicated that the dark strips were twin bands. A careful examination also revealed fine stacking fault fringes parallel to the length of the bands, although the fringes were difficult to see due to the interference from the strain field around defect clusters. The widths of twin bands (top and bottom surfaces of the foil) in Fig. 3(b) appear narrower than those in (a), because the twin bands are positioned at a steeper angle relative to the foil. When the bands in Fig. 3(b) were imaged edge-on by tilting further, deformation channels appeared to be cleaner [Fig. 3(c)], because defect clusters on either side of the channel were not imaged in the channel band. Moreover, the contrast of the line dislocations on the glide planes became weak or out-of contrast for edge-on conditions when the Burgers vectors on the glide planes were perpendicular to the diffracting vector **g** (i.e., $\mathbf{g}\cdot\mathbf{b} = 0$). A significant fraction of defects were cleared in the channel bands but some still remained. An important finding was that twin bands, stacking fault fringes, and defect-reduced channels were all manifestations of the same microstructure, which were revealed differently by varying the imaging conditions. This is further demonstrated below.

Figure 4 shows the deformation microstructures produced by tensile test (20% strain) for 316LN stain-

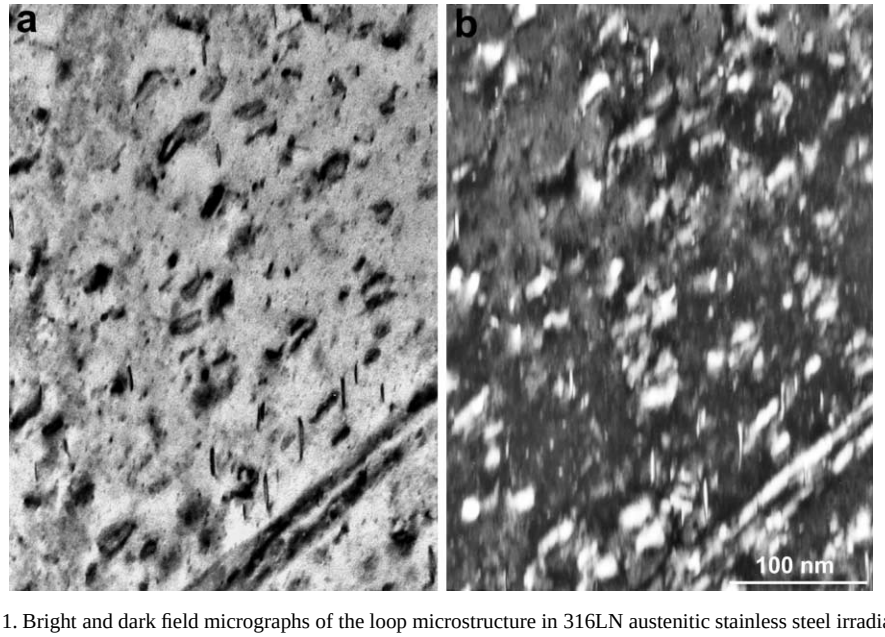

Fig. 1. Bright and dark field micrographs of the loop microstructure in 316LN austenitic stainless steel irradiated to 10 dpa at 200°C with 3.5 MeV Fe ions. The beam direction is near $\mathbf{B}\approx[111]$.

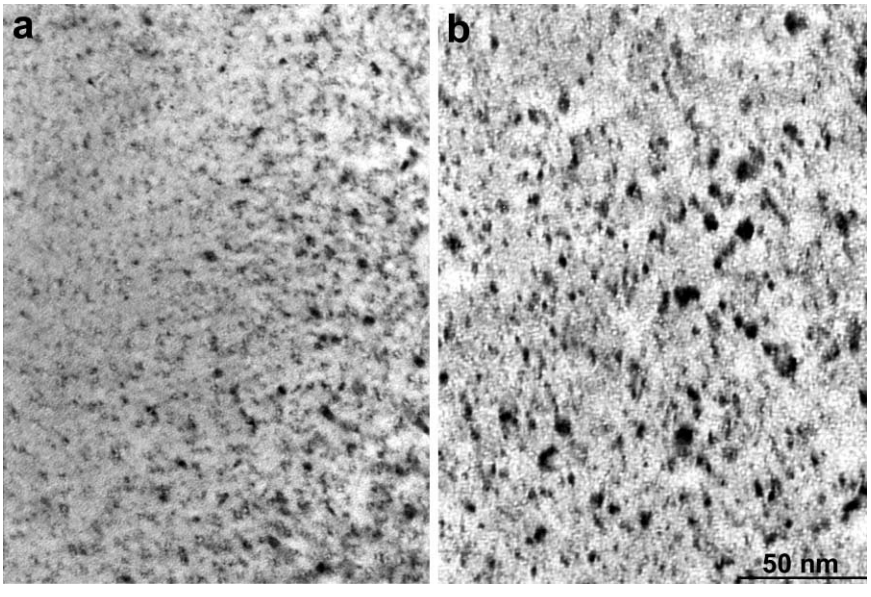

Fig. 2. Bubble and loop microstructures in 316LN austenitic stainless steel irradiated to (a) 5 at.% He (3.75 dpa) and (b) 10 at.% He (7.5 dpa) at 200°C with 360 keV He. The beam direction is **B**≈[100].

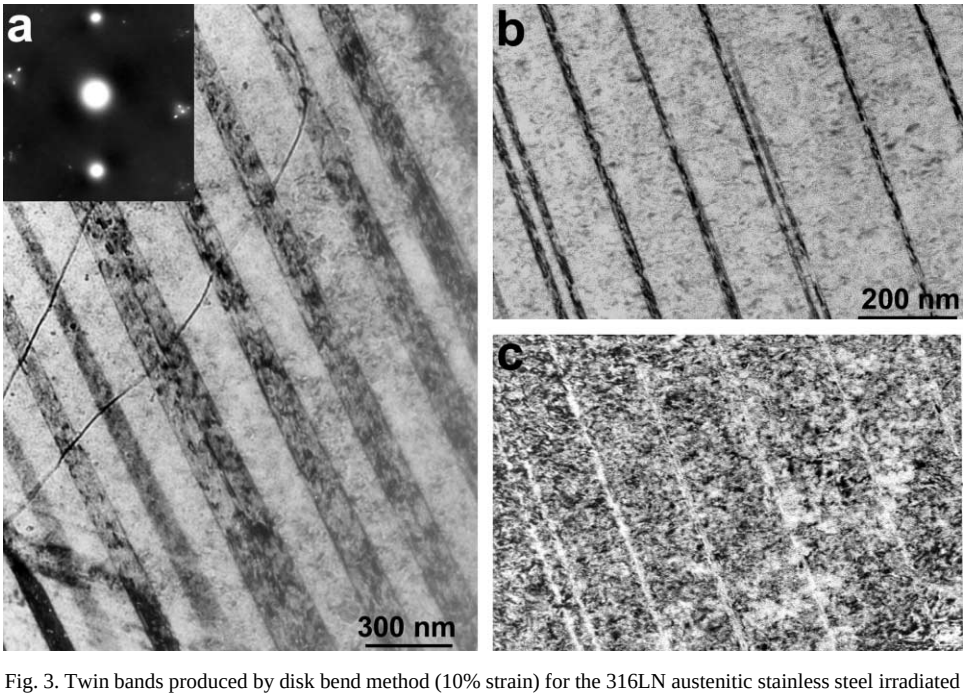

Fig. 3. Twin bands produced by disk bend method (10% strain) for the 316LN austenitic stainless steel irradiated at 200°C (a) to 10 dpa with 3.5 MeV Fe and (b) irradiated to 7.5 dpa (10 at.% He) with 360 keV He, and (c) deformation channels with reduced defects were imaged edge-on by tilting the twin bands shown in (b).

less steel irradiated to 10 dpa at 200°C with 3.5 MeV Fe together with 360 keV He (200 appm He/dpa) and 180 keV H (1000 appm/dpa), simultaneously. The micrographs were taken by varying tilt angles to show that the same deformation bands could be imaged in various ways. Figure 4(a) was taken at a beam direction near **B**≈[110], where the twin bands lay on two different (111) planes that were slightly tilted from the perpendicular beam direction. The twins are generally a composite of several atomic thick twin layers, so we call them nanotwins. Dark and bright contrasts in the twin band marked by an arrow indicated that the twin band was a composite of many overlapping nanotwins or faults bounded by Shockley partial dislocations; the detailed relation between twin and Shockley partial dislocations is described in Part II of this paper. Figure 4(b) shows the stacking fault fringes obtained from the twin bands shown in (a) at

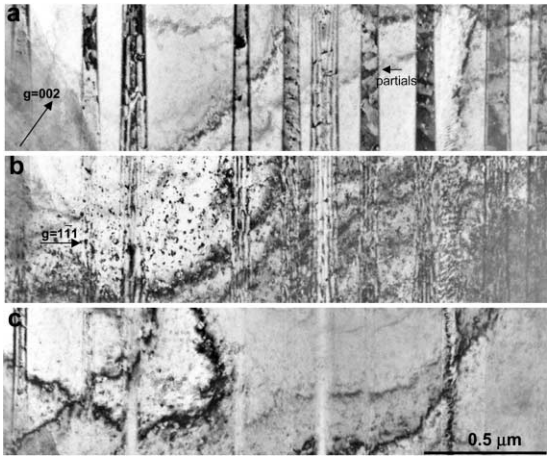

Fig. 4. Twin bands (a), stacking fault fringes (b), and defect-reduced channels (c) imaged from the same deformation bands for 316LN stainless steel irradiated by triple-ion beams and tensile tested at room temperature to 20% strain. Irradiation was done at 200°C with 3.5 MeV Fe (10 dpa), 360 keV He (200 appm/dpa), and 180 keV H (1000 appm/dpa) triple ion beams.

a different diffracting condition. The defect-reduced channels in (c) were imaged by tilting the twin bands to a near edge-on condition, and so the band widths appeared narrower.

One of the most notable observations was that dislocations on glide planes tended to separate more readily into Shockley partial dislocations with increasing ion dose. Figure 5 shows dislocations on glide planes for the specimens irradiated at 200°C to various doses with 360 keV He and strained to 10% by the disk bend method. In the unirradiated condition in Fig. 5, most dislocations on glide planes had

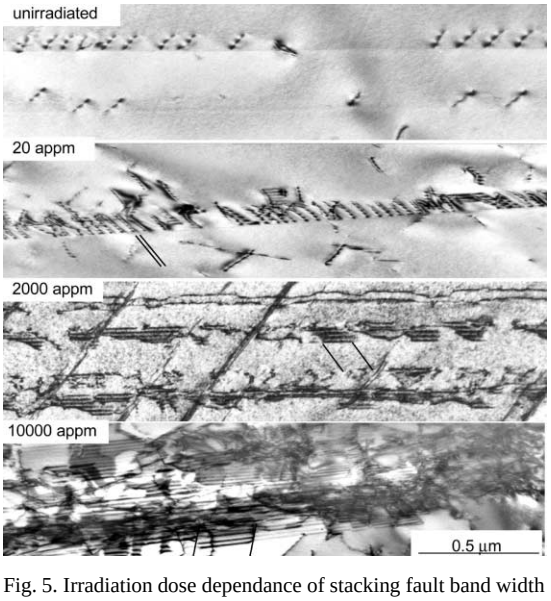

Fig. 5. Irradiation dose dependance of stacking fault band width in 316 LN austenitic stainless steel irradiated to various helium levels with 360 keV He ions at 200°C and strained to 10% by disk-bend test method.

$\mathbf{b} = \langle 110 \rangle/2$ type Burgers vectors. With increasing helium dose, however, not only did each dislocation separate into Shockley partial dislocations, but also the distance between the two pairing partials tended to increase as indicted by the three sets of parallel lines in Fig. 5.

Detailed analysis was carried out to understand the nature of Shockley partials for the 20 appm He implanted specimen in Fig. 6 and Table 1. A careful examination indicated that the piled-up dislocations on a glide plane (marked by 'B') were in pairs as shown in the magnified inset at the bottom left of Fig. 6(a). The dislocation pairs marked by '+' and '−' signs at the upper part of the micrograph were the same type as those marked by 'B', but were dislocations with opposite Burgers vectors that were moving in opposite directions. Another notable observation was that the stacking fault fringes marked by 'A' showed a dislocation line on the top side of the fringes at the diffracting condition of $\mathbf{g} = (\bar{1}11)$ in Fig. 6(a) but the dislocation line appeared at the bottom side of the fringes when the diffracting condition was changed to $\mathbf{g} = (1\bar{1}1)$ in Fig. 6(b). Here, the foil normal was near $\mathbf{B} \approx [110]$, parallel to the electron beam for both diffracting conditions. The Burgers vectors of the Shockley partials marked by 'A' and 'B' were determined by using the visibility criteria of $\mathbf{g} \cdot \mathbf{b} = \pm 2/3$ [24]. The results are summarized in Table 1 at the top and bottom three rows for 'A' and 'B' type partials, respectively. The partials marked by 'A' were on a (111) plane and resulted from the dissociation of a perfect dislocation with $\mathbf{b} = [1\bar{1}0]/2$, and those marked by 'B' were on $(11\bar{1})$ planes and resulted from the dissociations of perfect dislocations with $\mathbf{b} = [011]/2$. The corresponding dissociation reactions are as follows.

$$\frac{1}{2}[1\bar{1}0] \rightarrow \frac{1}{6}[2\bar{1}\bar{1}] + \frac{1}{6}[1\bar{2}1] \tag{1}$$

$$\frac{1}{2}[011] \rightarrow \frac{1}{6}[\bar{1}21] + \frac{1}{6}[112]. \tag{2}$$

The deformation bands in a highly strained region consisted of many overlapping bands of nanotwins or stacking faults bounded by Shockley partial dislocations on adjacent or nearly adjacent slip planes. Figure 7 shows an example of piled-up dislocations near a grain boundary in the 1 at.% He implanted and 10% strained specimen. The widths of stacking fault fringe bands (regions bounded by two paired Shockley partial dislocations) became narrower due to constriction near the grain boundary. Stacking fault fringes were in contrast when the phase angle $\phi = 2\pi \mathbf{g} \bullet \mathbf{R}$ had nonzero or non-integer values [24]. In the f.c.c. structure, the displacement vector ($\mathbf{R}$) normal to the stacking faulted plane is $\mathbf{R} = \pm[111]/3$. The contrast of some stacking fault fringes are out of contrast in the regions where normal stacking is restored by the overlap of

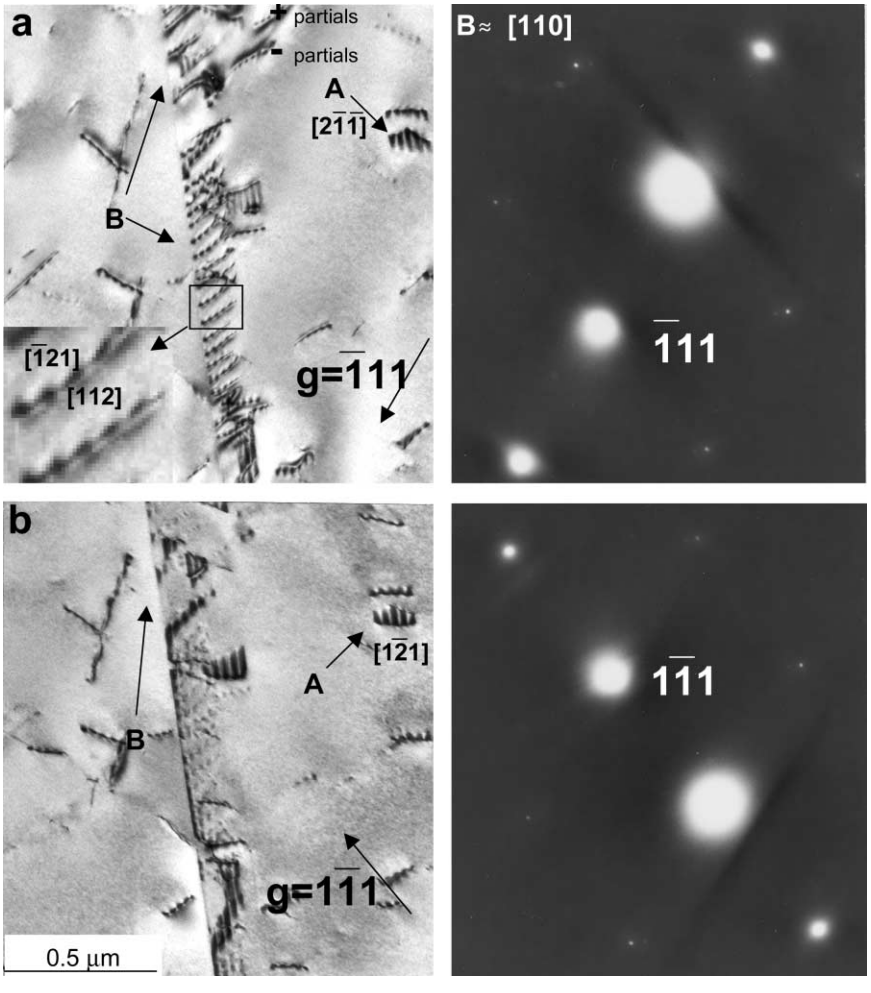

Fig. 6. Shockley partial dislocations in 316LN stainless steel irradiated to 20 appm (0.0015 dpa) at 200°C with 360 keV He. The micrographs were taken near the beam direction of **B**≈[110] with a diffraction conditions of (a) **g** = ($\bar{1}$11) and (b) **g** = (1$\bar{1}$1).

Table 1. Values of **g·b** for the partial dislocations corresponding to Fig. 6 for the foil normal near **B**≈[110] parallel to the electron beam. The three partials in the first row are on a (111) plane and the three partials in the fourth row are on ($\bar{1}$11) planes. The criteria of visibility (**g·b**=±2/3) and invisibility (**g·b**=±1/3) indicate that the Burgers vectors of the partials marked by 'A' are [2$\bar{1}$1]/6 and [$\bar{1}$21]/6 and those marked by 'B' are [112]/6 and [$\bar{1}$21]/6. The satisfied conditions in determining the Burgers vectors are indicated by the **bold** numerals. Note that both partials marked by 'B' are out of contrast (**g·b** = + 1/3 and −1/3) at the diffracting condition of **g** = ($\bar{1}$11) in Fig. 6 (b), so it cannot be [2$\bar{1}$1]/6 which should be visible (**g·b** = 2/3) at **g** = (1$\bar{1}$1)

'A' partials	plane **b**→$\frac{1}{3}$[111]	$\frac{1}{6}$**[2$\bar{1}\bar{1}$]**	$\frac{1}{6}$**[1$\bar{2}\bar{1}$]**	$\frac{1}{6}$[$\bar{1}\bar{1}$2]
g = $\bar{1}$1$\bar{1}$	$\frac{1}{3}$	**−$\frac{2}{3}$**	−$\frac{1}{3}$	$\frac{1}{3}$
g = 1$\bar{1}$1	$\frac{1}{3}$	$\frac{1}{3}$	$\frac{2}{3}$	$\frac{1}{3}$
'B' partials	plane **b**→$\frac{1}{3}$[11$\bar{1}$]	$\frac{1}{6}$**[11$\bar{2}$]**	$\frac{1}{6}$**[$\bar{1}$21]**	$\frac{1}{6}$[2$\bar{1}$1]
g = $\bar{1}$1$\bar{1}$	−$\frac{1}{3}$	$\frac{1}{3}$	$\frac{2}{3}$	−$\frac{1}{3}$
g = 1$\bar{1}$1	−$\frac{1}{3}$	$\frac{1}{3}$	**−$\frac{1}{3}$**	$\frac{2}{3}$

three successive displacements, i.e., **R** = 3×[111]/3, which is a perfect lattice vector, and it thus appeared to give 2π**g•R** = 0. Thus, stacking fault fringes can disappear for every third layer if three stacking faults overlap successively. An example is shown in Fig. 7 where the out of contrast stacking fault fringes are marked by the numbers '3' in the circled area of the micrograph.

Finally, the stacking-fault formation was not unique to the irradiated specimens. Extensive faults were also observed in an unirradiated specimen at a highly strained condition. Figure 8 illustrates various

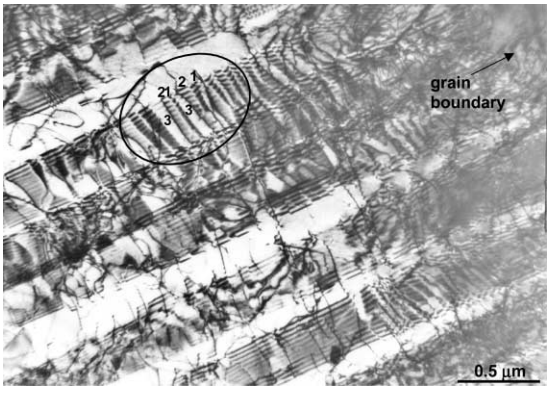

Fig. 7. Bands of stacking fault fringes formed by piled-up Shockley partial dislocations in 316LN stainless steel irradiated to 1 at.% He with 360 keV He at 200°C and strained to 10% at room temperature by the disk bend method. Note the disappearing stacking fault fringes for every third layer in the region marked by the numbers.

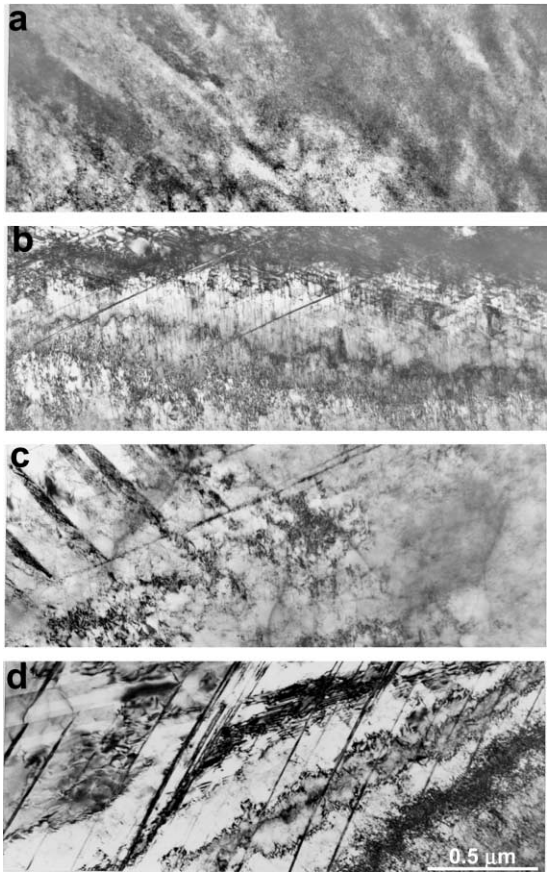

Fig. 8. Deformation microstructure in 316 LN austenitic stainless steel strained to 20% at room temperature by an uniaxial tensile test. The micrographs were obtained from the same perforated hole indicating that the deformation is non-uniform.

microstructures for an unirradiated specimen tensile tested to 20% strain at room temperature. The micrographs were taken from different areas around the same perforated hole in a TEM specimen. As mentioned in the experimental section, the dislocation microstructures were rather non-uniform from area to area and showed various stages of deformation in the same specimen or even in the same grain, (a) heavily tangled dislocations, (b) forest dislocations, and (c, d) twin bands at two different areas. Figure 9 shows a heavily faulted area in the same specimen. The micrographs were taken from the same deformation bands at various imaging conditions, (a) stacking fault fringes, (b) twin bands, (c) twin bands near edge-on, and (d) defect-reduced channels. Here, the channels appeared clean when $\mathbf{g}\cdot\mathbf{b} = 0$ (weak contrast) was satisfied for the pileup dislocations on glide planes by tilting the twin bands to edge-on. As the strain level increases, network dislocations and glide dislocations begin to interact producing jogs at the intersections. Since the jogs produced by the leading partial make the dislocations less mobile, the trailing partial tends to separate from the leading partial. This is believed to be the cause of extensive fault formation in heavily strained conditions. Detailed dislocation interaction mechanisms are discussed in Part II of this paper.

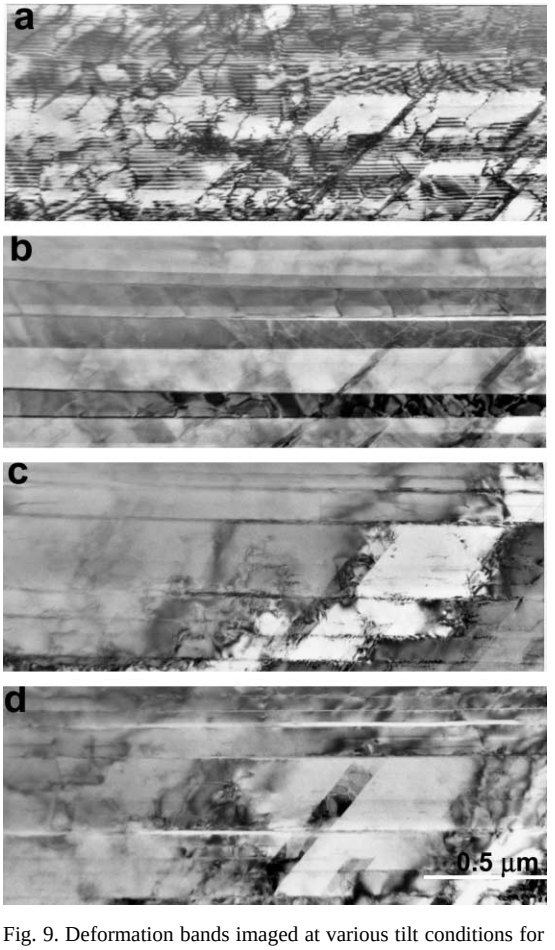

Fig. 9. Deformation bands imaged at various tilt conditions for the same 20% strained 316 LN shown in Fig. 8: (a) stacking fault fringes, (b) twin bands, (c) narrowed twin bands by tilting, and (d) channel bands imaged in the edge-on condition.

4. CONCLUSIONS

Deformation microstructures were characterized by TEM for AISI 316 LN austenitic stainless steel irradiated at 200°C with 160 keV H, 360 keV He and/or 3.5 MeV Fe ions and subsequently strained at room temperature by disk bend or tensile test methods. The results showed that glide dislocations dissociated into Shockley partial dislocations that increase in separation with increasing irradiation dose and increasing strain. The enhanced planar glide ensued during deformation because it is difficult for pinned and widely separated Shockley partial dislocations to cross-slip. Nanotwins and stacking fault ribbons were a consequence of stacking violation between the two separated Shockley partial dislocations. Defect-reduced channels resulted from the clearing of defects by the passage of Shockley partial dislocations. Consequently, deformation bands consist of piled-up dislocations, nanotwins, stacking faults, and defect-reduced channels all tied up together. The visual appearance of each component of a deformation band can be isolated and enhanced by simply changing the imaging condition in TEM.

Although all the deformation tests in this work were conducted at room temperature, the deformation microstructures were similar to those obtained under a wide range of test conditions [10–14]. Specifically, the irradiated and deformed austenitic stainless steels showed the same types of deformation microstructures regardless of irradiation sources (i.e., neutron, proton, heavy ions), test methods (i.e., disk bend, tensile), and temperature from liquid nitrogen temperature to 450°C based on currently available data and on-going study. In this regard, the observations and analyses made in this work are considered to be valid in the temperature range reported by other workers for deformation studies of stainless steels with f.c.c. structure and low stacking fault energy. However, deformation modes may be different at very low or high temperatures and for materials with high stacking fault energy or different crystal structure such as Cu, Al, Mo, V, Nb etc. In high stacking fault energy materials or in b.c.c. crystals, defect-reduced channels may form without involving twin formation. These are the subjects of future investigation. A final remark is that since disk-bending produces qualitatively similar deformation microstructures as tensile strain, it can be a powerful and economical means of studying deformation mechanisms for both irradiated and unirradiated materials. In Part II of this paper, the origin of deformation microstructures and associated mechanisms are discussed in detail.

Acknowledgements—Research sponsored by the Division of Materials Sciences and Engineering, Office of Basic Energy Sciences, US Department of Energy, under contract No. DE-AC05-00OR22725 with UT-Battelle, LLC. The authors wish to thank Drs E. A. Kenik and S. J. Zinkle for reviewing the manuscript.

REFERENCES

1. Bruemmer, S. M., Cole, J. I., Carter, R. D. and Was, G. S., *Mat. Res. Soc. Symp. Proc.*, 1997, **439**, 437.
2. Pawel, J. E., Rowcliffe, A. F., Alexander, D. J., Grossbeck, M. L. and Shiba, K., *J. Nucl. Mater.*, 1996, **202**, 233.
3. Maloy, S. A., James, M. R., Sommer, W. F., Fergueson, P., Wilcutt, G., Alexander, D., Loutan, Jr., M. R., Hamilton, M. L., Snead, L. and Sokolov, M. A., in *Proc. 3rd Int. Topical Meeting on Nuclear Applications of Accelerator Technology*, Long Beach, CA, AccApp'99. American Nuclear Society, La Grange, IL, 1999, pp. 541.
4. Wechsler, M. S., in *The Inhomogeneity of Plastic Deformation*. American Society for Metals, Metals Park, OH, 1971, p. 18, Chap. 2.
5. Nathanson, P. D. K., Jackson, P. J. and Spalding, D. R., *Acta Metall.*, 1980, **28**, 823.
6. Jin, Z. and Bieler, T. R., *Phil Mag.*, 1995, **71**, 925.
7. Bay, B., Hansen, N., Hughes, D. A. and Kuhlmann-Wilsdorf, D., *Acta metall. mater.*, 1992, **40**, 205.
8. Sharp, J. V., *Phil. Mag.*, 1967, **16**, 77.
9. Sharp, J. V., *Acta metall.*, 1974, **22**, 449.
10. Bloom, E. E., in *Radiation Damage in Metals*. American Society for Metals, Metals Park, OH, 1975, p. 295.
11. Cole, J. I. and Bruemmer, S. M., *J. Nucl. Mater.*, 1995, **225**, 53.
12. Suzuki, M., Sato, A. and Mori, T., *Phil. Mag.*, 1992, **65**, 1309.
13. Bailat, C., Groschel, F. and Victoria, M., *J. Nucl. Mater.*, 2000, **276**, 283.
14. Hashimoto, N., Zinkle, S. J., Rowcliffe, A. F., Robertson, J. P. and Jitsukawa, S., *J. Nucl. Mater.*, 2000, NUMA 14112,??.
15. Lee, E. H., Byun, T. S., Hunn, J. D., Hashimoto, N. and Farrell, K., *J. Nucl Mater.*, 2000, **281**, 65.
16. Byun, T. S., Lee, E. H., Hunn, J. D., Farrell, K. and Mansur, L. K., *J. Nucl. Mater.*, to be submitted.
17. Ziegler, J. F., Biersack, J. P. and Littmark, U., *The Stopping and Range of Ions in Solids*. Pergamon Press, Oxford, 1985.
18. Norgett, M. J., Robinson, M. T. and Torrens, I. M., *Nucl. Eng. Design*, 1975, **33**, 50.
19. Lee, E. H., *Nucl. Instrum. Meth. Phys. Res. B*, 1999, **151**, 29.
20. Tabor, D. J., *Hardness of Metals*. Clarendon Press, London, 1951.
21. Mansur, L. K. and Yoo, M. H., *J. Nucl. Mater.*, 1979, **85-86**, 523.
22. Lee, E. H., Hunn, J. D., Hashimoto, N. and Mansur, L. K., *J. Nucl. Mater.*, 1999, **278**, 266.
23. Lee, E. H., Hunn, J. D., Byun, T. S. and Mansur, L. K., *J. Nucl. Mater.*, 2000, **280**, 18.
24. Williams, D. B. and Carter, C. B., *Transmission Electron Microscopy*. Plenum Press, New York, 1996.